(Received 8 October 2023, Accepted 12 January 2024, Scheduled 25 January 2024)

Vibro-Acoustic Analysis for Transformer under DC Bias Based on Electromagnetic Coupling

Chao Pan, Xiaobo Shi*, Tongrui Fu, and Jingge An

Key Laboratory of Modern Power System Simulation and Control & Renewable Energy Technology Ministry of Education (Northeast Electric Power University), Jilin 132012, China

ABSTRACT: Aiming at the operational stability of DC-biased transformer, a multi-parameter correlation method based on electromagnetic coupling is presented in this paper. The mode-state analysis scheme is designed, and the feature parameters of electromagnetic, mechanical, and acoustic fields in internal components are simulated and analyzed. The electromagnetic properties under DC bias are simulated by the electromagnetic model, thus the winding current and magnetic flux density are extracted as the feature parameters. Then the vibration and stress distribution can be solved by the mechanical model, which are treated as the feature parameters of the mechanical field. By utilizing the computed mechanical information as excitation, the spatial-temporal distribution of sound pressure can be obtained in the acoustic model. Taking three-phase three-limb transformer and three-phase group transformer as examples, the electromagnetic, mechanical, and acoustic parameters of components are analyzed under different conditions. The variations of feature parameters are summarized and contrasted. Furthermore, actual vibration and noise parameters are measured through dynamic experimental platforms. The effectiveness of the multi-parameter correlation method is verified by the consistency between simulation and experiments, and the unobservable abnormal physical features can be represented by observable electrical information.

1. INTRODUCTION

1.1. Background

DC disturbance problem is focused on in modern artificial networks, such as electronized power system [1], railway traction [2], monopolar-ground mode of high voltage direct current (HVDC) [3], and geomagnetic storm [4]. This problem will lead to the magnetic bias phenomenon of transformer in AC power system. In recent years, there has been frequent occurrence of large-scale blackouts in power systems worldwide due to DC disturbance on transformers. With DC disturbance, transformer takes unstable performance of excitation saturation, current distortion, harmonic increase, etc. [5, 6]. These situations are accompanied by abnormalities such as vibration and noise, which will affect the equipment and environment, and even endanger the system security and reliability [7, 8].

1.2. Literature Review and Motivation

In [9], DC bias experiments are carried out to analyze the audible noise of DC-biased transformer. In [10], the vibration and noise of transformer are analyzed by finite element method, and the results show that the frequency band of noise pressure level is mainly distributed in 100 Hz and 200 Hz. In [11], the vibration and noise of transformer under DC bias are analyzed considering the magnetostriction of transformer silicon steel sheets. In [12], two 500 kV transformers are used for DC bias experiments, providing a reference for further research into noise characteristics of large power transformers. In summary, the existing literature is mostly devoted to the preliminary study of the mechanical stability and noise of transformer components. However, the intrinsic correlation of electromagnetic, vibration, and acoustic propagation under DC bias condition is not thoroughly researched. Moreover, it is a critical issue in equipment monitoring that the unobservable abnormal physical features can be difficultly represented by observable electrical information.

1.3. Main Methods and Contributions of This Work

In this study, the vibro-acoustic characteristics of DC-biased transformer are analyzed based on electromagnetic-mechanical-acoustic sequential coupling. Electromagnetic characteristics are researched with finite element, and the stress of winding and core can be solved. The electromagnetic-mechanical coupling model is carried out to solve the vibration acceleration of components. Then the spatial-temporal distribution of sound pressure can be simulated by mechanical-acoustic coupling model with the vibration acceleration as excitation source. Meanwhile, the vibration acceleration and noise are measured by experimental platforms to verify the simulation results. Finally, the operating states of DC-biased transformer are evaluated, and the instability criterion is further discussed.

The primary contributions are as follows: 1) A multi-parameter correlation method is proposed to comprehensively analyze the impact of DC disturbance on the transformer components. Based on electromagnetic theory, the electromagnetic-mechanical-acoustic coupling model is

* Corresponding author: Xiaobo Shi (568431772@qq.com).

built. Through the aforementioned method and model, the intrinsic correlation and potential laws among the multi-field characteristics of DC-biased transformer are studied and revealed, which will be helpful for condition monitoring and assessment of devices in practice. 2) Through virtual simulation and dynamic experiments, the instability criteria for the transformer under DC disturbance are summarized. The unobservable abnormal vibration and noise can be represented by observable DC disturbance and load factor, which provides a basis for anomaly identification and situational awareness of equipment.

2. MODE-STATE ANALYSIS BASED ON ELECTRO-MAGNETIC-MECHANICAL-ACOUSTIC COUPLING FOR DC-BIASED TRANSFORMER

The mathematical model of mode-state analysis in time domain for DC-biased transformer is established based on electromagnetic-mechanical-acoustic coupling.

$$\begin{cases} \mathbf{S_e} = \mathbf{S_e}(t_k, L, i, B) + \mathbf{E} \cdot \mathbf{Input_e}(t_k, U_{\mathbf{AC}}, \boldsymbol{\xi}) \\ \mathbf{Output_e}(t_k, i, B, F) = \boldsymbol{\Gamma} \cdot \mathbf{S}_e \\ \mathbf{S_m} = \mathbf{S_m}(t_k, g) + \mathbf{M} \cdot \mathbf{Input_m}(t_k, \boldsymbol{\zeta}_{\mathbf{e-m}}) \\ \mathbf{Output_m}(t_k, g) = \boldsymbol{\gamma} \cdot \mathbf{S_m} \\ \mathbf{S_c} = \mathbf{S_c}(t_k, p) + \mathbf{C} \cdot \mathbf{Input_c}(t_k, \boldsymbol{\zeta}_{\mathbf{m-c}}) \\ \mathbf{Output_c}(t_k, p) = \boldsymbol{\tau} \cdot \mathbf{S_c} \end{cases} \tag{1}$$

$$\begin{cases} \boldsymbol{\xi} = (\mathbf{I_{DC}}, \boldsymbol{\eta}) \\ \boldsymbol{\zeta} = (\boldsymbol{\zeta}_{\mathbf{e-m}}, \boldsymbol{\zeta}_{\mathbf{m-c}}) = (\mathbf{F}, \mathbf{g}) \end{cases} \tag{2}$$

where **S** is the system state matrix which contains electromagnetic/mechanical/acoustic state matrix $\mathbf{S_e}$/$\mathbf{S_m}$/$\mathbf{S_c}$. With time t as a link index, multi-field information in **S** changes accordingly, such as inductance L, winding current i, flux density B, electromagnetic force F, vibration acceleration g, and sound pressure p. **Input** is the system input matrix which contains electromagnetic/mechanical/acoustic input matrix $\mathbf{Input_e}$/$\mathbf{Input_m}$/$\mathbf{Input_c}$. **E**, **M**, and **C** are input coefficient matrices. U_{AC} is sinusoidal AC excitation. ξ is control parameter matrix which contains DC disturbance $\mathbf{I_{DC}}$ and load factor $\boldsymbol{\eta}$. ζ is coupling correlation matrix, containing electromagnetic-mechanical coupling parameter $\zeta_{\mathbf{e-m}}(\mathbf{F})$ and mechanical-acoustic coupling parameter $\zeta_{\mathbf{m-c}}(\mathbf{g})$. **Output** is the system output matrix that contains multi-field output matrix $\mathbf{Output_e}$/$\mathbf{Output_m}$/$\mathbf{Output_c}$. $\boldsymbol{\Gamma}$, $\boldsymbol{\gamma}$, and $\boldsymbol{\tau}$ are extracting matrices, which extract feature parameters from **S** to construct **Output**.

2.1. Electromagnetic Model

The magnetic-circuit parameters of transformer are computed by the electromagnetic coupling.

2.1.1. Magnetic Model

Assuming that excitation currents in windings are known, inductance matrix **L** can be computed through Energy Balance Finite Element Method (EBFEM), which is on the basis of magnetic vector potential **A**. Furthermore, the magnetic model can be solved by Galerkin [13].

$$\nabla \times (v\nabla \times \mathbf{A}) = \int \mathbf{J} dV \tag{3}$$

$$G_a = \int_V \nabla \times \mathbf{M}_m \cdot (v\nabla \times \mathbf{A}) dV - \int_{Vc} \mathbf{M}_m \cdot \mathbf{J} dV - \int_s \mathbf{M}_m \cdot [(v\nabla \times \mathbf{A}) \times \mathbf{n}] dS \tag{4}$$

where v is the magnetic reluctivity. **A** is the magnetic vector potential. **J** is the current density. G_{a} is the Galerkin residuals. $\{\mathbf{M}_m\}$ is the sequence of weight function, and the basis function is identical to the weight function. **n** is the normal component.

A system of algebraic equations is obtained by discretizing the G_{a} equation, then **A** and some field parameters can be solved, such as magnetic flux density **B** and magnetic field energy W of the winding and core.

$$\mathbf{B} = \nabla \times \mathbf{A} \tag{5}$$

$$dW_1 = \frac{1}{2} \int d\mathbf{B} \cdot d\mathbf{H} \tag{6}$$

where **H** is the magnetic field intensity.

Taking three-phase group transformer as an example, the variation of primary/secondary winding currents at a certain moment is $di_{\mathrm{p}}/di_{\mathrm{s}}$ ($p,\ s = 1, 2$).

$$dW_2 = \frac{1}{2} L_{ps} di_p di_s \tag{7}$$

Time-domain inductance can be computed through EBFEM. Making W_1 equal to W_2, then Equations (6) and (7) can be linked. Thus, magnetic and circuit parameters are associated with calculating **L**, which is taken as the state variable of the circuit model. The above inductance calculation method is applied to three-phase three-limb transformer, which will not be described due to space limitations.

2.1.2. Circuit Model

The calculated **L** is feedback to the circuit model, then the winding currents can be solved. Assuming that DC injects from the primary side, the model of Yd-type three-phase group transformer with DC disturbance is illustrated in Fig. 1.

Ignoring the leakage inductance of each winding, loop equations of DC-biased three-phase group transformer can be obtained as follows (The derivation process of Yd-type three-phase three-limb transformer is similar to the three-phase group

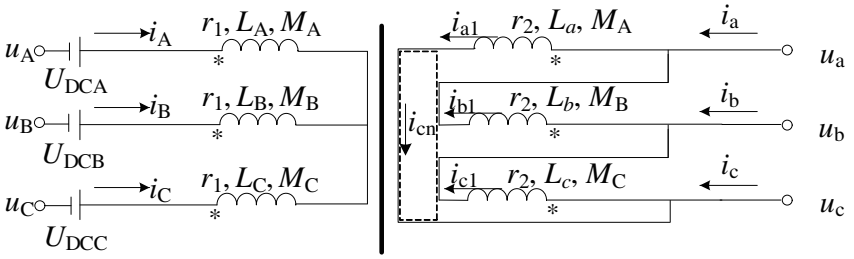

FIGURE 1. DC disturbance circuit of three-phase group transformer.

transformer).

$$\begin{cases} \begin{bmatrix} u_A \\ u_B \\ u_C \end{bmatrix} = \begin{bmatrix} i_A \\ i_B \\ i_C \end{bmatrix} r_1 + \begin{bmatrix} L_A & & \\ & L_B & \\ & & L_C \end{bmatrix} \begin{bmatrix} \cdot \\ i_A \\ \cdot \\ i_B \\ \cdot \\ i_C \end{bmatrix} \\ + \begin{bmatrix} M_A & & \\ & M_B & \\ & & M_C \end{bmatrix} \begin{bmatrix} \cdot \\ i_{a1} \\ \cdot \\ i_{b1} \\ \cdot \\ i_{c1} \end{bmatrix} - \begin{bmatrix} U_{DCA} \\ U_{DCB} \\ U_{DCC} \end{bmatrix} \\ \begin{bmatrix} u_a \\ u_b \\ u_c \end{bmatrix} = \begin{bmatrix} i_{a1} \\ i_{b1} \\ i_{c1} \end{bmatrix} r_2 + \begin{bmatrix} L_a & & \\ & L_b & \\ & & L_c \end{bmatrix} \begin{bmatrix} \cdot \\ i_{a1} \\ \cdot \\ i_{b1} \\ \cdot \\ i_{c1} \end{bmatrix} \\ + \begin{bmatrix} M_A & & \\ & M_B & \\ & & M_C \end{bmatrix} \begin{bmatrix} \cdot \\ i_A \\ \cdot \\ i_B \\ \cdot \\ i_C \end{bmatrix} \end{cases} \tag{8}$$

where i_{A}, i_{B}, and i_{C} are the primary winding currents. i_{a1}, i_{b1}, and i_{c1} are the secondary delta currents. i_{a}, i_{b}, and i_{c} are the secondary port currents. i_{cn} is the secondary loop current. u_{A}, u_{B}, and u_{C} are the primary voltages. u_{a}, u_{b}, and u_{c} are the secondary voltages. r_1 and r_2 are the winding resistances. $L_{\mathrm{A}}/L_{\mathrm{B}}/L_{\mathrm{C}}$ and $L_{\mathrm{a}}/L_{\mathrm{b}}/L_{\mathrm{c}}$ are the primary/secondary self-inductances. $M_{\mathrm{A}}/M_{\mathrm{B}}/M_{\mathrm{C}}$ are the mutual inductances. U_{DCA}, U_{DCB}, and U_{DCC} are the DC sources.

L at time t_k is substituted into the circuit differential equations, then the winding current i_k at t_k can be obtained. Furthermore, the winding current at the next moment is solved through Fourth-order Runge-Kutta Method (RK4) in the circuit model.

$$i_{k+1} = i_k + \frac{h}{6}\left(s_1 + 2s_2 + 2s_3 + s_4\right) \tag{9}$$

where h is the time step. $s_1 \sim s_4$ are the slopes of piecewise calculation.

2.2. Mechanical Model

The electromagnetic force on the component can be calculated through the solved parameters in electromagnetic model.

$$\mathbf{F}_k = \frac{\partial W}{\partial k} = \int \mathbf{B}\frac{\partial \mathbf{H}}{\partial k} dV \tag{10}$$

where $\mathbf{F}_{\mathrm{k}}$ is the electromagnetic force of coil or iron core in the direction k, and the definition range of $\mathbf{k}$ is $\{x, y, z\}$.

The electromagnetic force applied to transformer windings can be decomposed into radial and axial components [14]. In this study, the vibration characteristics of winding with axial electromagnetic force are mainly researched. Virtual model of transformer winding is constructed based on the mass-spring-damping system, as shown in Fig. 2 [15].

In Fig. 2, rigid mass m stands for the pie winding; insulation pad is represented by a spring; and coil damping is represented by a damper. The insulation pads are subjected to pre-tightening force, which is defined as $\mathbf{F}_b$. The mathematical model for axial vibration of winding is established [16].

$$nm\mathbf{g} + \sum_{1}^{n} C\mathbf{v} + \left[K_f + \sum_{1}^{n-1} K + K_e\right]\mathbf{d} = \mathbf{F}_w + \mathbf{G}_w \tag{11}$$

where n is the number of winding coils. m is the mass of winding coils. C is the damping coefficient. K_f, K, and K_e are the stiffness coefficients of head, middle, and end pads, respectively. **d**, **v**, and **g** are the displacement vector, velocity vector, and acceleration vector of winding node, respectively. $\mathbf{F}_w$ and $\mathbf{G}_w$ are the force and gravity of transformer winding. Considering the stiffness characteristics of insulation pads and winding coils, the material properties are considered linear when the pre-tightening force is constant [17].

Due to the magnetostriction of the ferromagnetic materials, the arrangement of the magnetic domains changes, leading to the vibration of iron core in alternating magnetic field [18]. Therefore, the magnetostriction of core is the main cause of vibration. Relevant principle and formulas of magnetostrictive effect are shown in Appendix A [19, 20].

As shown in Fig. 3, an ideal vibration equivalent mass unit of the iron core is established, in which **x** is the axial displacement of the iron core, and $\mathbf{F} + \mathbf{dF}$ is the force on the cross section of core column. The cross-sectional area of the core column can be considered equal everywhere. Therefore, the motion equation of iron core vibration can be obtained through force anal-

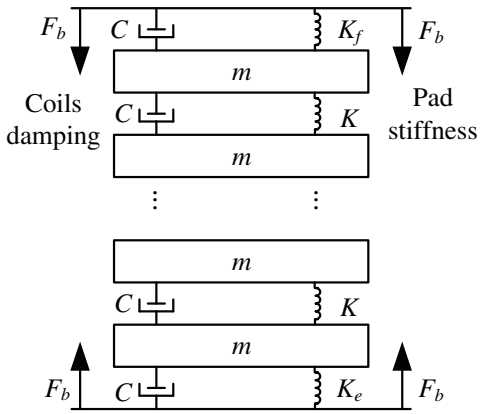

FIGURE 2. Mass-spring-damping system of winding.

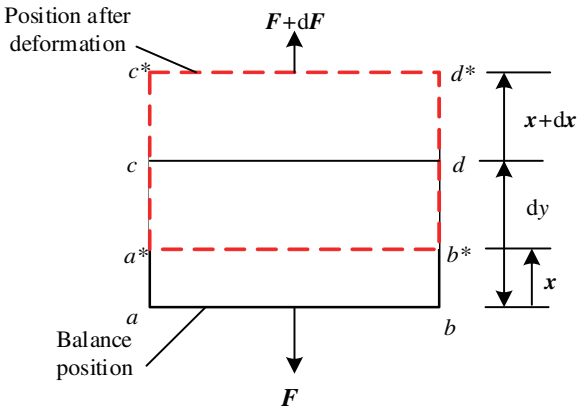

FIGURE 3. Vibration equivalent mass unit of core.

ysis and derivation.

$$ES_c\frac{\partial^2\mathbf{x}\,(y,t)}{\partial y^2}+\mathbf{f}\,(y,t)=\rho S_c\frac{\partial^2\mathbf{x}\,(y,t)}{\partial t^2} \tag{12}$$

where E is the Young's modulus. $\partial\mathbf{x}/\partial\mathbf{y}$ is the axial strain. $\mathbf{f}(y,t)$ is the magnetostrictive force on this mass unit. y and t are position and time, respectively. ρ is the iron core density, and S_c is the cross-sectional area.

2.3. Acoustic Fluctuation Model

Since the vibration acceleration g is calculated by the mechanical model, it is used as the excitation of the acoustic model.

$$\begin{cases} -\mathbf{n}\cdot\left(-\frac{1}{\rho_a}(\nabla p_t-\mathbf{q}_d)\right)=-\mathbf{n}\cdot\mathbf{g} \\ p_t=p_b+p_n \end{cases} \tag{13}$$

where ρ_a is the air fluid density. p_t, p_b, and p_n are total sound pressure, background sound pressure, and transformer noise pressure, respectively. $\mathbf{q}_d$ is the dipole domain source.

The acoustic model can be solved in time domain:

$$\frac{1}{\rho_a c^2}\frac{\partial^2 p_t}{\partial t^2}+\nabla\cdot\left(-\frac{1}{\rho_a}\left(\nabla p_t-\mathbf{q}_d\right)\right)=\mathbf{Q} \tag{14}$$

where c is the speed of sound, and $\mathbf{Q}$ is the unipolar domain source.

With the sound pressure level L_p, the sound pressure variations are analyzed:

$$L_p=20\cdot\lg\left(\frac{P}{P_{ref}}\right) \tag{15}$$

where the unit of L_p is decibel (dB). P is the valid value of sound pressure. P_{ref} is the reference value of sound pressure, which is generally taken as 20 μPa.

2.4. Multi-Parameter Correlation Based on Multi-Field Sequential Coupling

The flowchart of multi-parameter correlation method based on multi-field sequential coupling is shown in Fig. 4, and the constructure steps are as follows:

Step 1: A dynamic information database for multi-physics virtual simulation is built. With time set as a link index, electromagnetic information at t_k is retrieved from the electromagnetic sub-information database. Inductance parameters (calculated by EBFEM in magnetic field model) at t_k are substituted into the circuit differential equations, then the winding current i_k at t_k can be obtained. i_k is input as the excitation in current-carrying domain and magnetic connected domain. Meanwhile, the DC disturbance I_{DC} and load factor η are defined as control parameters, which is set as mode label in the dynamic link database. Then the electromagnetic spatial-temporal distribution of transformer is solved to obtain the feature parameters such as main flux and leakage.

Step *2*: When the absolute convergence norm is less than the criterion value or the coupled cycle reaches the maximum of constraints, the iterative process ends. Links are established according to the time index, and the calculation results are stored in the global multi-field information database. Conversely, i_k updates to i_{k+1} through RK4 in the circuit model, and i_{k+1} is input into the magnetic field model. Then the feature parameters of magnetic field will be solved at the next moment.

Step *3*: Based on the electromagnetic coupling, the spatial-temporal distribution of electromagnetic force F is obtained, which will be dynamically stored with tag t_k. In the mechanical stress domain, F is taken as an excitation to obtain the vibration and acceleration g of winding and core. The information above is restored in the electromagnetic-mechanical sub-information database.

Step *4*: The mechanical information is retrieved from the multi-field information database at t_k. In the acoustic propagation domain, g_k is input as an excitation to obtain the sound pressure p of transformer. The feature parameter p is restored in the mechanical-acoustic sub-information database.

Step *5*: The dynamic link contains mode label (I_{DC}, η) and time index, enabling the construction of a global information database. The electromagnetic, mechanical, and acoustic in-

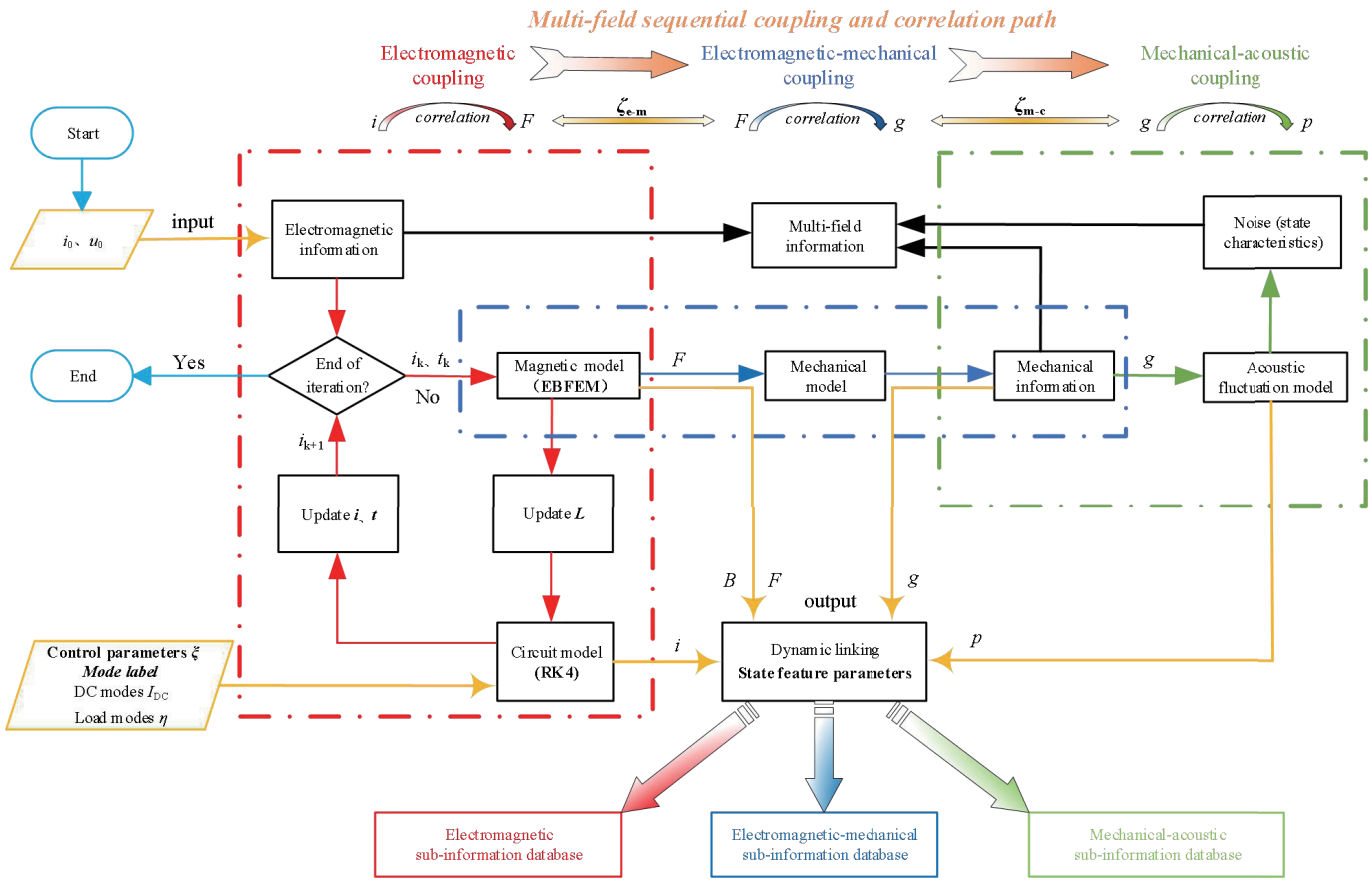

FIGURE 4. Multi-parameter correlation based on multi-field sequential coupling.

formation is merged to create a multi-field feature database for multi-parameter correlation.

3. SIMULATION

3.1. Three-Phase Three-Limb Transformer

3D finite element model is built based on an actual three-phase three-limb transformer named BSS-1000VA, as shown in Fig. 17. Material parameters such as Young's modulus and Poisson's ratio are measured by tensile-compression test. The specific parameters of transformer are shown in Table 1.

3.1.1. Pre-Procedure

For the numerical simulation based on sequential coupling of multi-physics field, toroidal current is input to the coil as excitation for electromagnetic model. The parallel outer boundary condition of magnetic induction is applied to the magnetic connected domain, while the natural boundary conditions are applied to other domains. In the mechanical stress domain, the pre-tightening force is applied as constant uniform distributed load according to the actual structure size of the experimental transformer. Fixed constraint is applied to the winding foundation, considering the axial component of winding vibration. The magnetostrictive effect is applied to the core. With the sound propagation boundary set to be a perfectly matched layer, the background sound pressure is set to 0 Pa.

Through the aforementioned settings, the preprocessing of the simulation model has been completed. The distinctions between the ideal simulation environment and real-world conditions are as follows: 1) In the real-world conditions, the winding and core of transformer are tightly fastened together, leading to mutual interference in vibration and noise propagation. In order to investigate and compare the multi-field characteristics of different components of transformers under DC disturbance, the winding and iron core are treated as independent entities in the ideal simulation environment. 2) In the real-world conditions, the noise monitoring data is influenced by the surrounding noise. The simulation model incorporates settings regarding the acoustic field, such as the perfectly matched layer, which eliminate interference from the aforementioned issues and enhance the accuracy of the acoustic field results.

A DC source is connected to the primary side of transformer, and different operating modes of transformer are set with DC disturbance which is defined as I_{DC}. By using an evaluating indicator h, the DC level is described as $I_{DC} = hI_0$, in which I_0 is the no-load current, and h can be 0, 0.5, 1.0, 1.5... Meanwhile, η is defined as load factor according to different load conditions. η can be 0, 25%, 50%, 75%, and 100%, respectively. The variations in electromagnetic-mechanical-acoustic fields under different h and η modes are simulated.

TABLE 1. Three-phase three-limb transformer parameters.

Parameters	Rated value	Measured value
Frequency/Hz	50	—
Capacity S_N/(VA)	1000	—
Voltage U_N/V	380/110	—
No-load current I_0/A	0.1	0.1
Core size/mm^3	—	190 × 190 × 44
Core window/mm^3	—	38 × 110 × 44
Number of turns of primary and secondary	497/251	—
Primary and secondary winding resistance/Ω	—	1.4/0.5
Young's modulus of silicon steel sheet/(10^5MPa)	—	1.93
Poisson's ratio of silicon steel sheet	—	0.26
Young's modulus of winding coils/(10^5MPa)	—	0.79
Poisson's ratio of winding coils	—	0.37

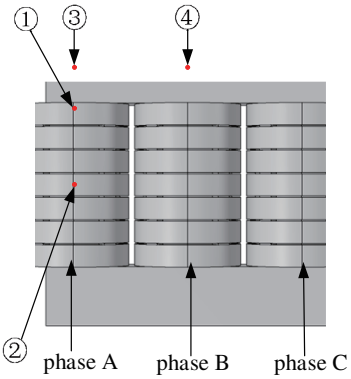

FIGURE 5. Measuring points arrangement for three-phase three-limb transformer.

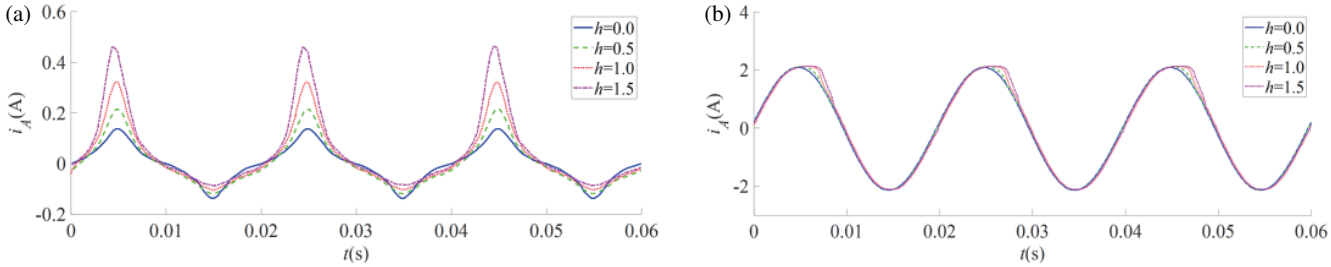

FIGURE 6. Primary winding current of phase A. (a) $\eta = 0$, (b) $\eta = 100\%$.

The arrangement of measuring points takes into account the structure features of three-phase three-limb transformer, as shown in Fig. 5.

3.1.2. Analysis of Simulation Results

i. Multi-Field Information of Winding

The variations of magnetic leakage density (B_L), force (F), and vibration acceleration (g) of winding in different modes are simulated. Taking phase A as an example, the information of each measuring point is shown in Fig. 8–Fig. 10. Partial results ($\eta = 0$ and 100%) of primary winding current and main flux are shown in Fig. 6 and Fig. 7.

Under no-load operation, the waveform and value of primary winding current are basically the same as the excitation current. The excitation saturation intensifies, and i_A becomes highly distorted with increasing h. In addition, the excitation feature of "half-wave distort, half-wave decay" is observed under no-load condition, as shown in Fig. 6(a). Under full-load operation, the numerical value of i_A is relatively large. Therefore, the distortion of i_A is not significant with DC disturbance.

As shown in Fig. 8, a typical bias phenomenon about leakage of "half-wave distort, half-wave decay" is observed at each measuring point under no-load condition. In loading modes, the

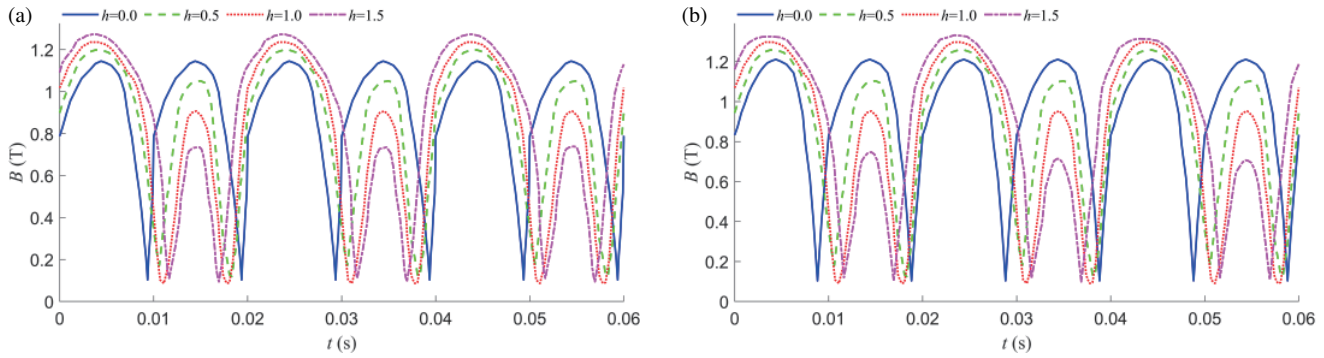

FIGURE 7. Main flux of phase A. (a) $\eta = 0$, (b) $\eta = 100\%$.

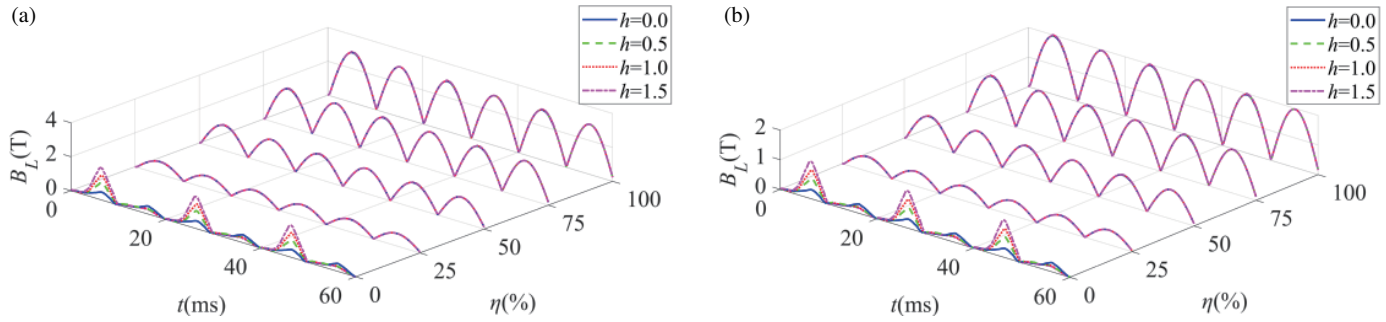

FIGURE 8. Magnetic leakage at measuring points of three-phase three-limb transformer winding. (a) Measuring point 1. (b) Measuring point 2.

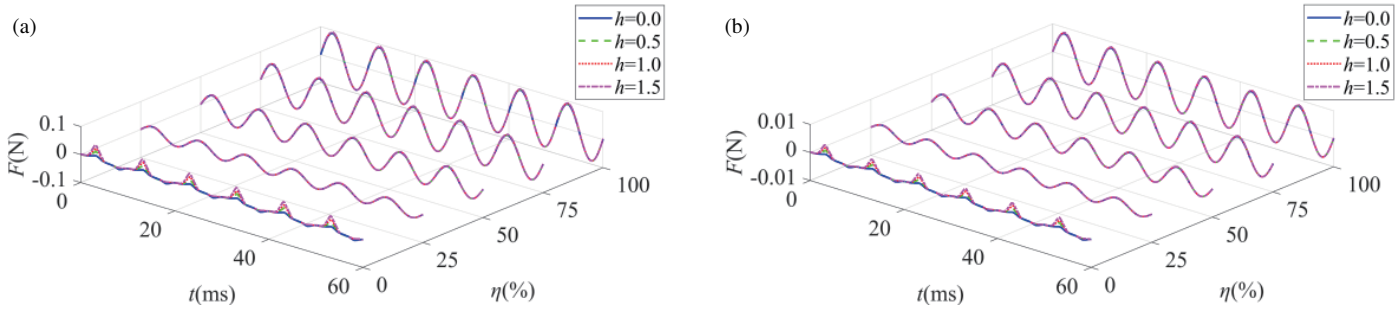

FIGURE 9. Electromagnetic force at measuring points of three-phase three-limb transformer winding. (a) Measuring point 1. (b) Measuring point 2.

leakage of the winding at different measuring points has similar variation, and the leakage increases with rising η. Moreover, the leakage at the terminal of winding is greater than the middle part. The reason is that leakage is mainly produced by alternating current in the winding. Thus, the variation of leakage is consistent with the current. Furthermore, the impact of DC disturbance on the winding current is relatively minor under loading condition, resulting in negligible distortion of the leakage. The variations of electromagnetic force are analyzed based on leakage, and the axial electromagnetic force at measuring points is extracted. The results are shown in Fig. 9.

In Fig. 9, the fluctuation period of electromagnetic force F is 0.5 times of the power frequency period. It is easy to see that F has similar variation at different measuring points. F at the terminal of winding is greater than the middle part. Furthermore, the distribution of F is consistent with the leakage, and F intensifies with rising η.

The variations of axial g at measuring points in windings are shown in Fig. 10.

As shown in Fig. 10, g at the terminal of pie winding is larger than the middle part, and g grows with rising η, whereas different DC has little effect on g under the same η. The reason is that g caused by F mainly depends on the leakage and current, which have no significant change with DC injecting in the loading operation. Thus, F and g are not closely related to the DC disturbance in loading modes.

By comparing Fig. 8–Fig. 10, it can be concluded that the leakage, electromagnetic force, and vibration acceleration of the winding have similar variation with the winding current.

ii. Vibration Information of Iron Core

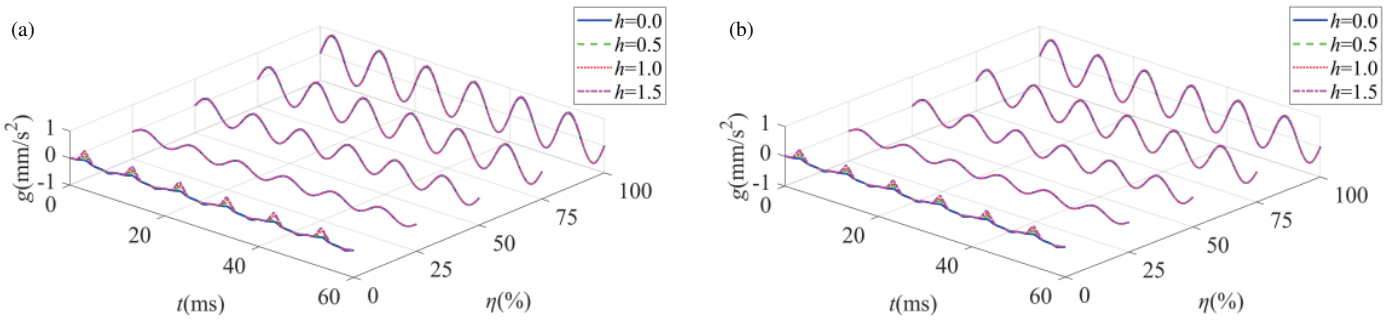

FIGURE 10. Vibration acceleration at measuring points of three-phase three-limb transformer winding. (a) Measuring point 1. (b) Measuring point 2.

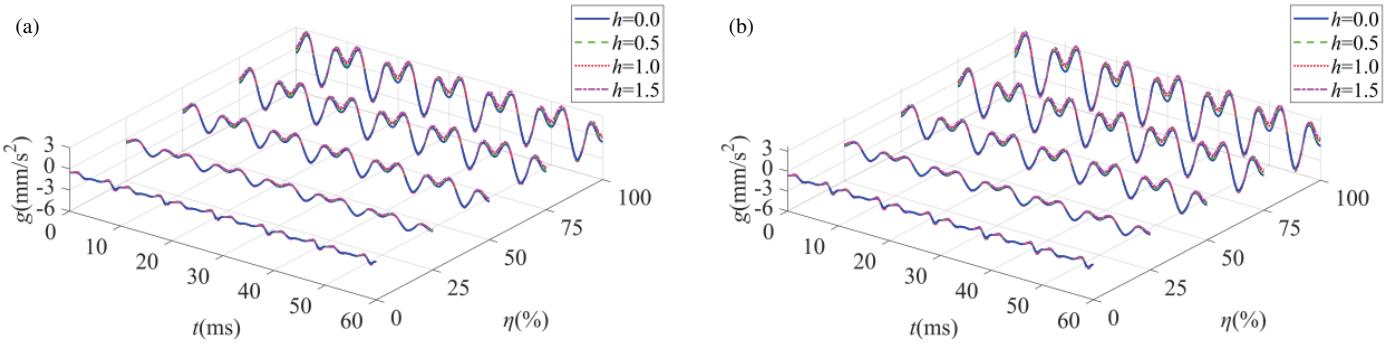

FIGURE 11. Vibration acceleration at measuring points of three-phase three-limb transformer core. (a) Measuring point 3. (b) Measuring point 4.

TABLE 2. Surface noise of three-phase three-limb transformer.

Noise \ Mode-state	h	η (%)				
		0	25	50	75	100
Surface p_1 (dB)	0	27.9	28.4	28.8	29.8	30.9
	0.5	28.2	28.7	29.1	30.3	31.5
	1.0	28.7	29.6	30.2	31.4	32.6
	1.5	29.9	30.8	31.5	32.8	34.1

On the other hand, the vibration problem of iron core in different load modes and DC modes is learned. In order to analyze the vibration characteristics of iron core at different positions, measuring points 3 and 4 are selected in Fig. 5. The results are shown in Fig. 11.

In Fig. 11, the vibration of iron core is more complex and violent than winding. In the same load mode, g increases with rising I_{DC}. In the same DC mode, g intensifies as η increases. Moreover, g of phase B is more violent than phase A with same η or I_{DC}.

Comparing Fig. 8–Fig. 11, it can be concluded that while the DC disturbance has little effect on the current and leakage of winding, it significantly affects the vibration of the iron core. The main reason is that DC injection generates corresponding DC flux in the core. As a result, the main flux of iron core is saturated in half period, and the excitation current is distorted severely, with significant vibration in iron core.

iii. Global Acoustic Information of Three-Phase Three-Limb Transformer

The maximum sound pressure level on the three-phase three-limb transformer is defined as p_1, as shown in Table 2.

The noise presents positive correlation with both h and η, which is consistent with the varying g. When η is 50%, and h is 0.5, the surface p_1 of internal components has nearly reached 30 dB. Taking no-load operation as an example, partial spatial-temporal distribution cloud charts of sound pressure and sound pressure level on the transformer are shown in Fig. 12 and Fig. 13.

As shown in Fig. 12, it is easy to see that the vibration of transformer components intensifies with increasing h, resulting in higher p. Furthermore, p of the core is significantly greater than the winding. The same phenomenon above can be found in other load modes, which will not be discussed in this paper due to space limitations.

In Fig. 13, the typical temporal distribution of sound pressure is researched, where $t = 20$ ms and 25 ms are the minimum and maximum moments of main flux in the distorted half-cycle respectively, and $t = 30$ ms and 35 ms are the minimum and maximum moments of main flux in the decaying half-cycle,

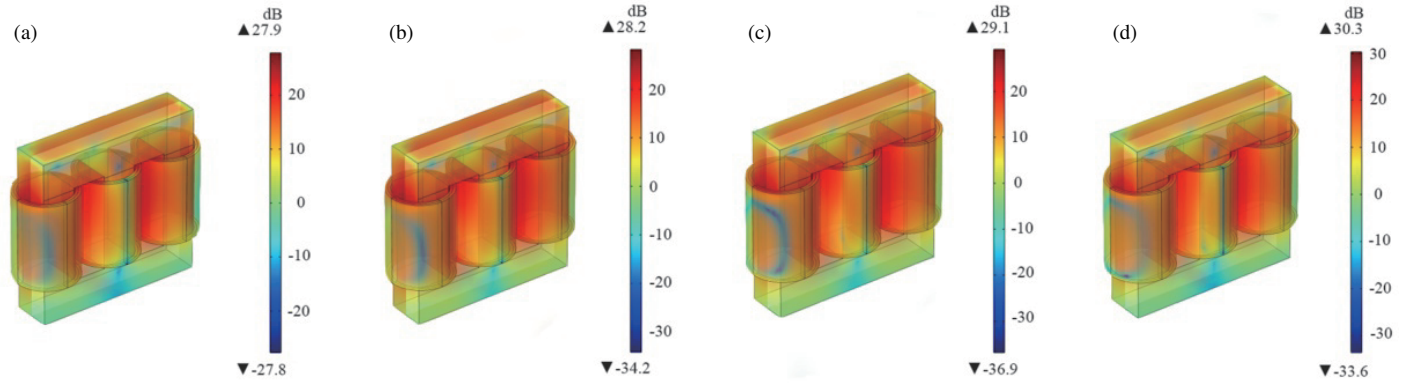

FIGURE 12. Spatial distribution of sound pressure level. (a) $h = 0$, (b) $h = 0.5$, (c) $h = 1.0$, (d) $h = 1.5$.

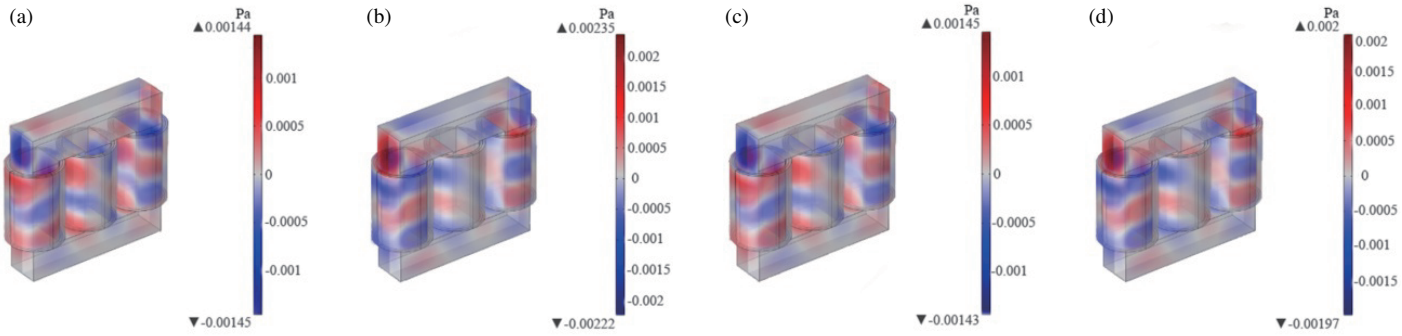

FIGURE 13. Temporal distribution of sound pressure. (a) $t = 20$ ms, (b) $t = 25$ ms, (c) $t = 30$ ms, (d) $t = 35$ ms.

TABLE 3. Three-phase group transformer parameters.

Parameters	Rated value	Measured value
Frequency/Hz	50	—
Capacity S_N/(VA)	1000	—
Voltage U_N/V	220/110	—
No-load current I_0/A	—	0.1
Core window (single phase)/mm^3	—	$120 \times 45 \times 105$
Number of turns of primary and secondary (single phase)	396/216	—
Primary and secondary winding resistance (single phase)/Ω	—	3.2/0.4
Young's modulus of silicon steel sheet/(10^5MPa)	—	1.93
Poisson's ratio of silicon steel sheet	—	0.26
Young's modulus of winding coils/(10^5MPa)	—	0.79
Poisson's ratio of winding coils	—	0.37

respectively. p at $t = 20$ ms and $t = 30$ ms are nearly the same, but p at $t = 25$ ms is greater than that at $t = 35$ ms, indicating the same variation with main flux.

3.2. Three-Phase Group Transformer

For comparative analysis, the simulation model of three-phase group transformer is built based on the rated parameters of the three-phase three-limb transformer. The specific parameters are shown in Table 3.

Taking into account the structure features of three-phase group transformer, phase A is selected for analysis. The arrangement of measuring points is shown in Fig. 14.

The winding currents of three-phase group transformer are simulated in different modes, and the variation laws are similar to that of three-phase three-limb transformer. Partial simulation results ($\eta = 0$ and 100%) of primary winding current are shown in Fig. 15.

The variations of B_L, F, and g at winding measuring points are simulated in different modes. Results (partial data are

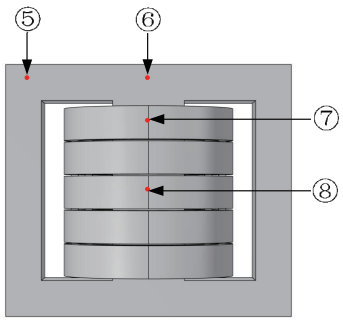

FIGURE 14. Measuring points arrangement for three-phase group transformer.

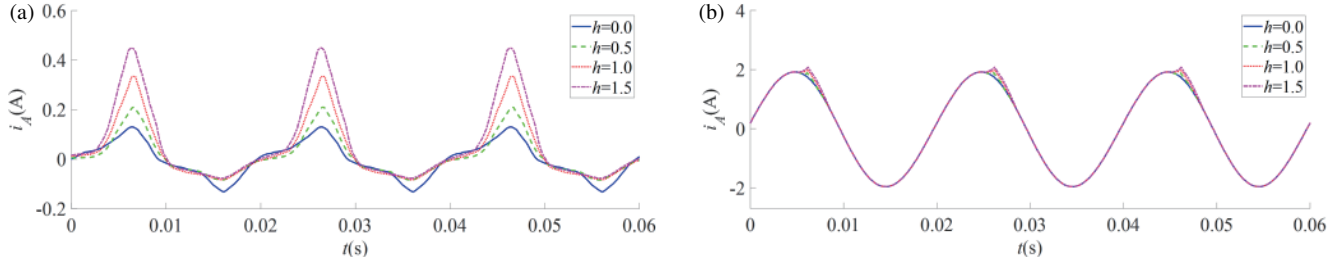

FIGURE 15. Primary winding current of phase A. (a) $\eta = 0$, (b) $\eta = 100\%$.

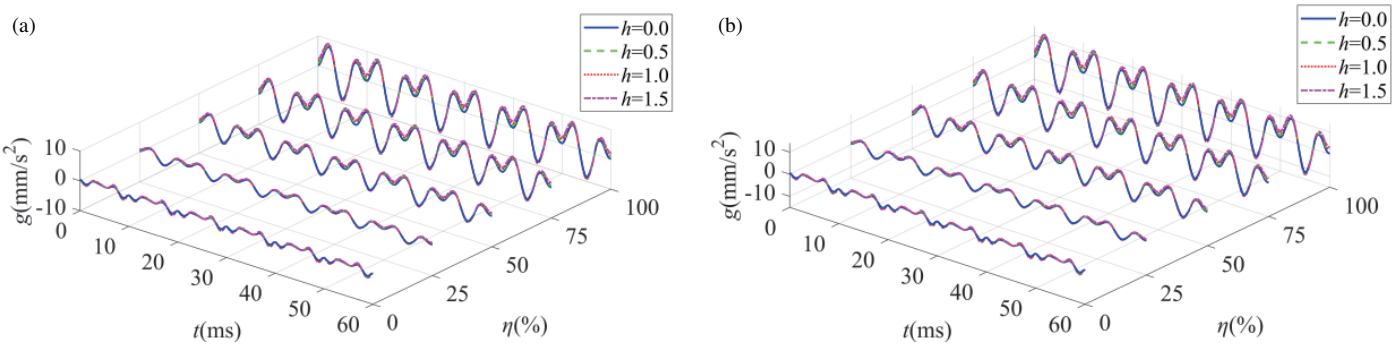

FIGURE 16. Vibration acceleration at measuring points of three-phase group transformer core. (a) Measuring point 5. (b) Measuring point 6.

TABLE 4. Surface noise of three-phase group transformer.

Noise \ Mode-state	h	η (%)				
		0	25	50	75	100
Surface p_2 (dB)	0	27.5	28.2	28.7	29.5	30.7
	0.5	28.3	28.9	29.6	30.8	32.3
	1.0	29.5	30.2	30.8	32.4	33.6
	1.5	30.1	31.8	31.9	33.2	34.9

shown in Appendix B) show that the variation of feature parameters above is similar with three-phase three-limb transformer. However, the variation of each parameter in three-phase group transformer is greater than three-phase three-limb transformer at the same DC level. Meanwhile, g of iron core is simulated, as shown in Fig. 16.

According to Fig. 16, it is easy to see that the vibration of the main iron column is more severe than the adjacent column. Comparing two types of transformers, the variation law of g in iron core is basically consistent. Moreover, they are both obviously affected by magnetostriction.

The maximum sound pressure level on the three-phase group transformer is defined as p_2, as shown in Table 4.

The noise of three-phase group transformer presents positive correlation with both h and η, which is consistent with the three-phase three-limb transformer. Comparing Table 2 and Table 4, p_1 and p_2 are nearly the same with no DC injection. However,

p_2 increases obviously with DC disturbance, and it is more drastic than p_1 in the same mode.

3.3. Summary of Simulation

The variation characteristics of transformer in bias effect are simulated, and laws are summarized.

1) With DC disturbance, the magnetic leakage, electromagnetic force, vibration acceleration, and current of transformer winding all have similar variation law. In no-load running, the fluctuation of multi-field information is significant with DC, which becomes weak under loading condition. With rising DC level, the vibration acceleration of iron core grows significantly. As load factor rises, the feature information of multi-physics increases.

2) In the ideal simulation environment, the vibration and propagation of the components do not interfere with each other. In the same DC or load mode, the vibration acceleration and noise of core are much greater than winding. Result shows that the vibration and noise of DC-biased transformer are mainly from iron core.

3) Comparing the simulation results of three-phase three-limb transformer and three-phase group transformer, it can be concluded that three-phase three-limb transformer has stronger resistance to DC disturbance.

4. EXPERIMENTS

As shown in Fig. 17, dynamic experimental platforms are built. The experimental transformer parameters are shown in Table 1 and Table 3, and the procedures are as follows.

Step 1: The voltage regulator T_1 and DC source are connected to the primary side of transformers, and the branch switch K is disconnected. The secondary side is connected to adjustable load. For the acquisition of electrical, vibration, and acoustic signals, different monitoring modules are adopted. In order to verify the simulation conclusions, the three-phase three-limb transformer vibration measuring points are consistent with simulation measuring points 1, 2, 3, and 4, and the three-phase group transformer vibration measuring points are consistent with simulation measuring points 5, 6, 7, and 8.

Step 2: K is closed. In voltage regulator module, T_1 is controlled to make the input excitation reach the rated voltage of primary side.

Step 3: DC source is set in DC injection module, and R_d is adjusted to control different DC disturbances.

Step 4: In electrical signal monitoring module, the voltage and current parameters are recorded.

Step 5: In vibration monitoring module, sensor JF2100-T (Sensitivity: 100mV/g, Frequency range: 10 Hz–10 kHz, Sampling frequency: 42 kHz) is used to collect core vibration signals under different DC levels. According to the noise test standard [21], transformer noise is measured by a sound level meter HS5671D+ (Frequency range: 26 Hz–20 kHz, Sampling frequency: 48 kHz) of noise monitoring module.

4.1. Three-Phase Three-Limb Transformer Dynamic Experiment

The vibration signals of three-phase three-limb transformer components are collected, and the axial information is extracted as shown in Fig. 18 and Fig. 19.

Actually, the vibration and propagation of internal components interfere with each other, so that the experimental waveforms are different from simulation. As a result, the measured signal contains more high-frequency components, which is more complex and serious than simulation. However, the experimental variation law of vibration acceleration g in windings is basically consistent with simulation. g at the terminal of winding is more violent than the middle part. As η increases, the vibration becomes more severe.

The vibration information of iron core is shown in Fig. 19.

In Fig. 19, the vibration of phase B is more violent than phase A. As η increases, g of iron core intensifies. Moreover, due to the nonlinear excitation and magnetostrictive characteristics, the vibration signal of core contains more high-frequency components, resulting in acute fluctuation in time domain. Meanwhile, it is important to note the occurrence of the "burr phenomenon", which can be attributed to experimental errors. It refers to the intense oscillation of the waveform, and values corresponding to smaller h are partly greater than those corresponding to larger h. However, the "burr phenomenon" does not affect the overall laws. In future research, we will utilize more precise measurement equipment to minimize the occurrence of errors.

The noise monitoring result is shown in Table 5.

Comparing Table 2 and Table 5, the measured noise p'_1 has the same variation trend with simulation p_1 in different modes. However, p'_1 is more drastic than p_1. It is found that p'_1 includes transformer noise and environmental noise. Furthermore, due to the nonlinear magnetic characteristics of iron core, the noise obtained from the experiment is found to be more intense. The results indicate that the variation law of noise is consistent with vibration. It is worth noting that when h is 1.0, obvious vibration and noise problems have occurred. When h is 2.0, the component vibration is serious, and the insulation is burned out.

4.2. Three-Phase Group Transformer Dynamic Experiment

The vibration signals of three-phase group transformer components are collected, and the axial information is extracted as shown in Fig. 20 and Fig. 21.

Similar to three-phase three-limb transformer, the experiment signals of three-phase group transformer are more violent than simulation. Meanwhile, the experimental variation law of g is basically consistent with simulation. The noise monitoring result is shown in Table 6.

Comparing Table 4 and Table 6, the measured noise p_2' is more drastic than simulation p_2, but p_2' has the same variation trend as p_2 in different modes. Furthermore, DC disturbance has more influence on three-phase group transformer, which can be learned by comparing Table 5 and Table 6.

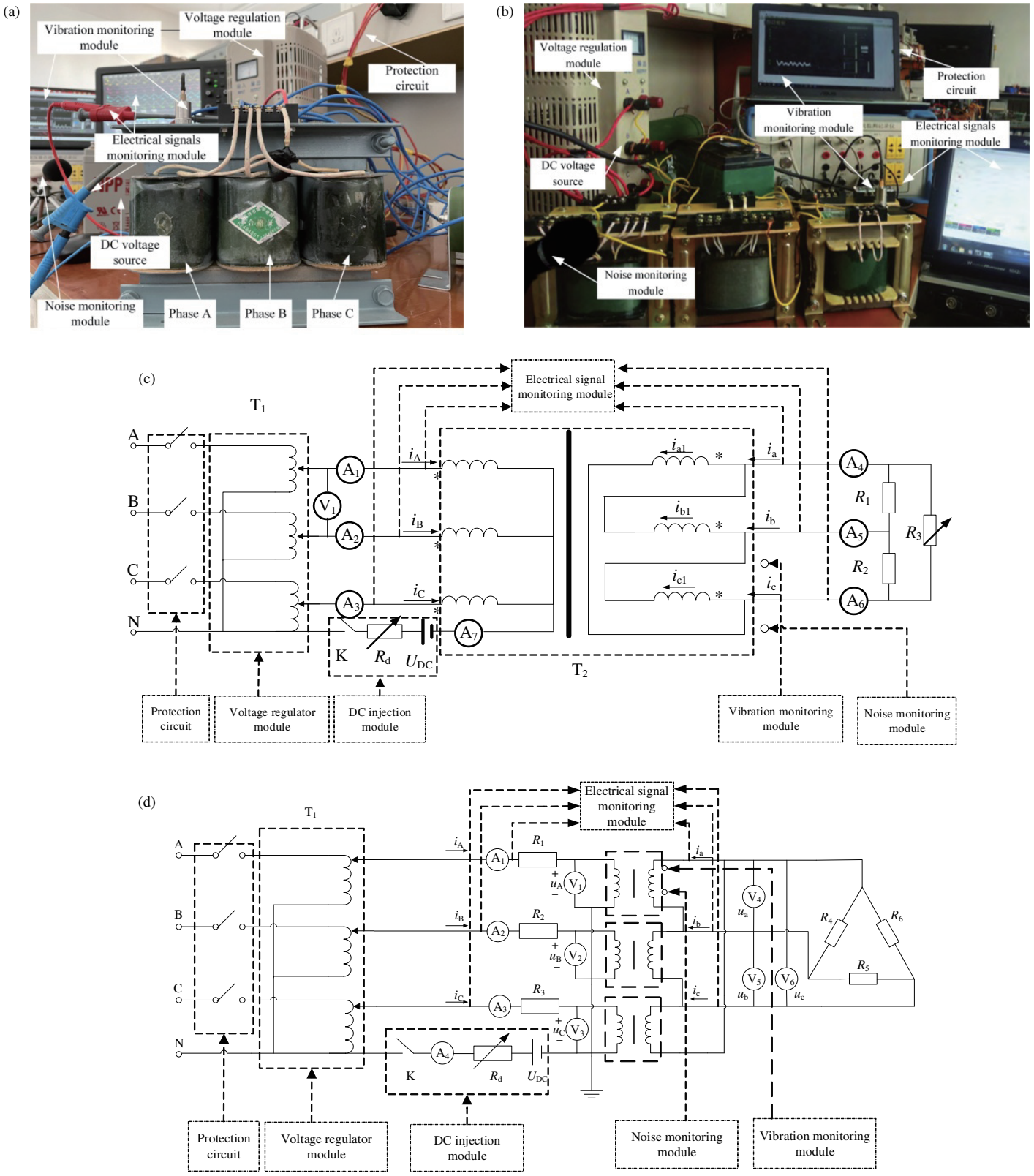

FIGURE 17. Dynamic experimental platform. (a) Physical experimental platform of three-phase three-limb transformer. (b) Physical experimental platform of three-phase group transformer. (c) Wiring of three-phase three-limb transformer experimental platform. (d) Wiring of three-phase group transformer experimental platform.

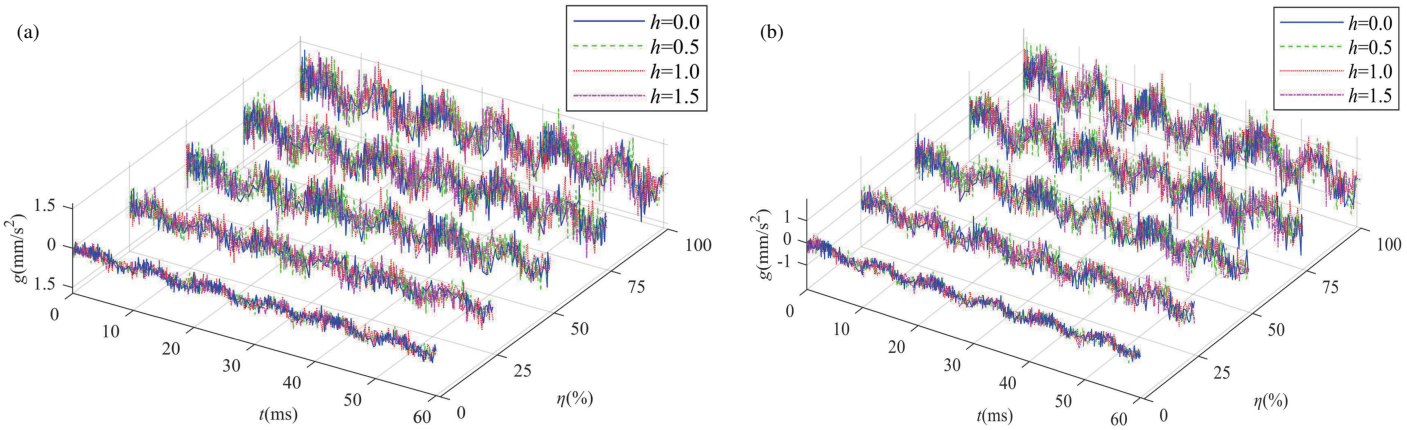

FIGURE 18. Vibration measurement of three-phase three-limb transformer winding. (a) Measuring point 1. (b) Measuring point 2.

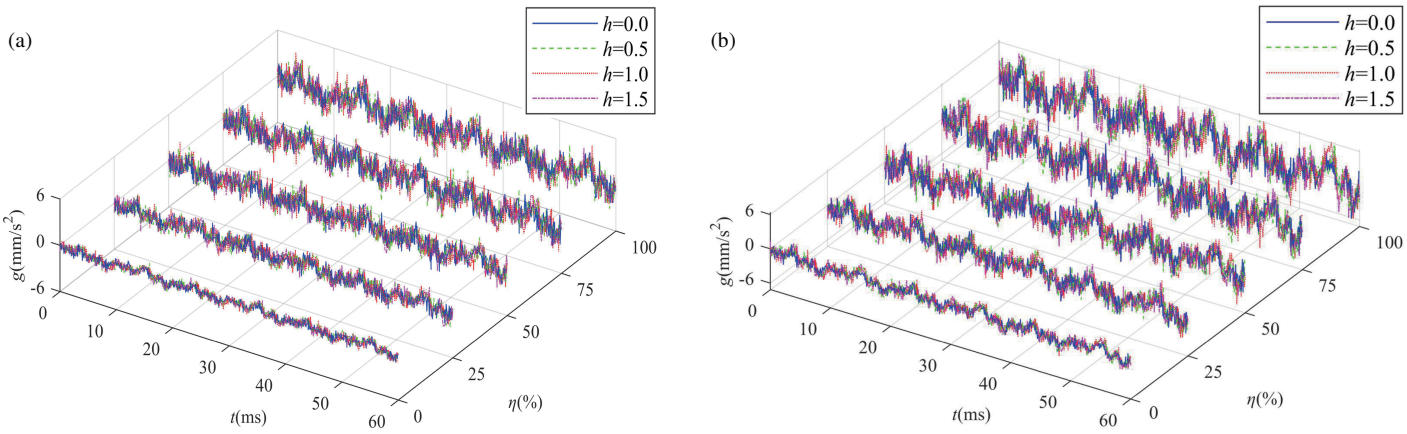

FIGURE 19. Vibration measurement of three-phase three-limb transformer core. (a) Measuring point 3. (b) Measuring point 4.

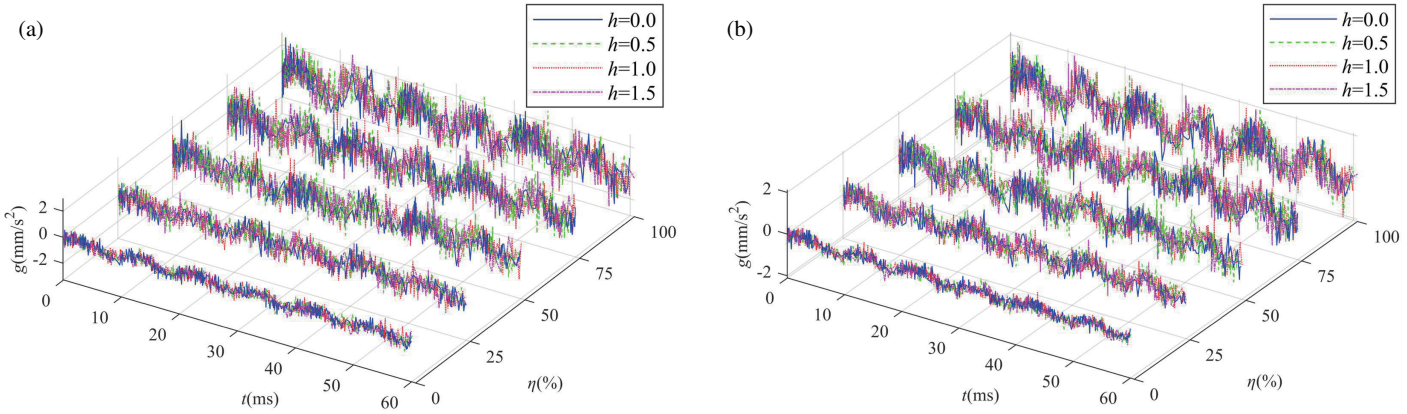

FIGURE 20. Vibration measurement of three-phase group transformer winding. (a) Measuring point 7. (b) Measuring point 8.

TABLE 5. Noise monitoring result of three-phase three-limb transformer.

Noise \ Mode-state	h	η (%)				
		0	25	50	75	100
Experimental p'_1 (dB)	0	29.4	30.9	31.3	32.5	33.6
	0.5	30.9	31.5	32.1	33.3	342
	1.0	31.4	32.1	33.1	34.2	35.6
	1.5	32.3	33.4	34.5	35.4	36.8

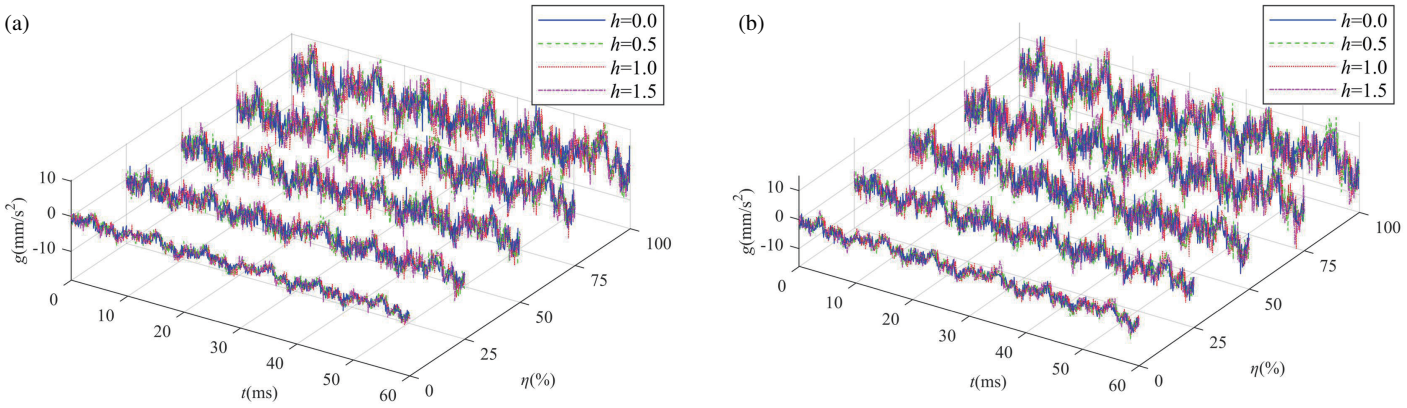

FIGURE 21. Vibration measurement of three-phase group transformer iron core. (a) Measuring point 5. (b) Measuring point 6.

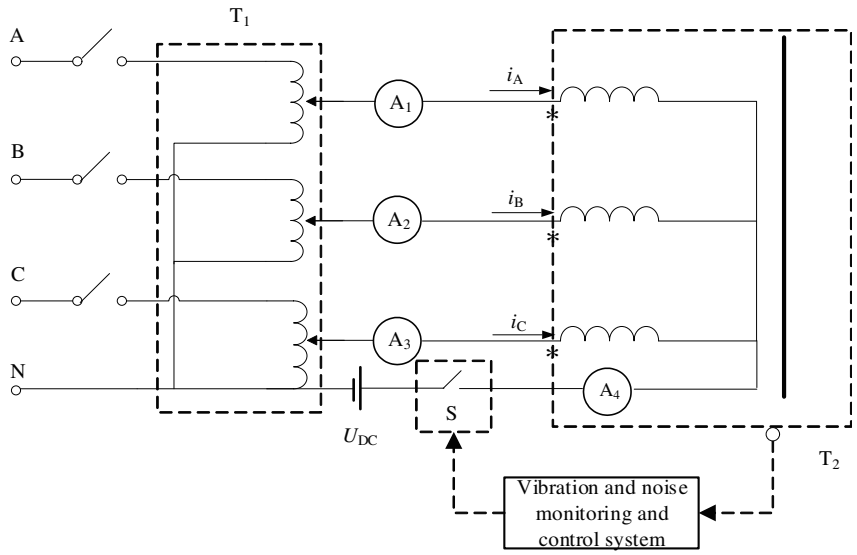

FIGURE 22. Suppression of transformer bias.

TABLE 6. Noise monitoring result of three-phase group transformer.

Noise \ Mode-state	h	η (%)				
		0	25	50	75	100
Experimental p_2' (dB)	0	29.2	30.8	31.2	32.4	33.4
	0.5	31.1	31.9	33.6	33.8	34.7
	1.0	32.5	32.8	34.0	34.6	36.0
	1.5	33.1	33.7	35.5	36.2	37.1

4.3. Discussion

On the basis of multi-field information analysis, instability criterion can be concluded.

1) Taking $\eta = 75\%$ for example, when $0 < h \leq 0.5$, the DC disturbance has little effect on the loading transformer. At this point, the DC level is within the permissible range of the transformer, indicating normal operation of the transformer.

2) When $0.5 < h \leq 1.5$, the DC disturbance has obvious influence on the electromagnetic compatibility and structure stability of transformer. At this point, the vibration and noise of the transformer components increase. If the transformer remains in this state for an extended period of time, it may result in problems such as bending deformation. Thus, there is an increased risk of instability, and more attention should be paid to it.

3) When $h \geq 2.0$, the transformer will be seriously affected by DC disturbance, accompanied by insulation burnout phenomenon. Its internal electromagnetic and mechanical environment has been unstable, which should be promptly alarmed and dealt with.

In actual operation, transformer generally takes load factor lower than 75%, and the current with DC disturbance is not up to the prewarning. However, serious problems of vibration and

noise have occurred in DC-biased effect, and other potential dangers may be encountered.

To solve the problems above, certain DC bias suppression should be taken. The switch module S at the neutral point of transformer is added as shown in Fig. 22. Vibration and noise are monitored in real time. When vibration or noise exceeds the set value, S is disconnected to avoid the influence of DC on the transformer. Another strategy is that DC disturbance can be isolated by connecting capacitors. However, the problem of nonlinear parametric oscillations needs to be considered, which will not be further discussed in this paper.

In allusion to the problem of transformer vibration noise, the monitoring method is generally tank sensing. Due to factors such as shielding, interference, and decay during the propagation of vibration noise, significant deviation will be caused in measurement. In this paper, the noise problem of transformer under DC bias is studied based on multi-field coupling. Through virtual simulation and physical experiments, the key characteristic information regarding electromagnetic, mechanical, and acoustic field is obtained. The results verify the spatial and temporal consistency of the multi-field physical characteristics. The feasibility of utilizing electrical parameters to represent noise anomalies is also demonstrated.

5. CONCLUSION

The vibration and noise are researched for three-phase three-limb transformer and three-phase group transformer in AC/DC hybrid environment on the basis of electromagnetic coupling. The conclusions are as follows:

With DC disturbance, the electromagnetic, mechanical, and acoustic field parameters of two types of transformers exhibit similar variation performance. The excitation feature of "half-wave distort, half-wave decay" is analyzed. The vibration and noise of transformer intensify with the rising DC disturbance or load factor. Moreover, the vibration and sound pressure level of iron core are stronger than winding in the same mode. The abnormal noise of DC-biased transformer is mainly caused by the core vibration. In addition, vibration and noise are more serious in three-phase group transformer, indicating that three-phase three-limb transformer has stronger resistance to DC disturbance.

Multi-physics sequential coupling model is suitable for DC-biased transformer analysis. The relationship between nonlinear excitation and multi-field morphology in bias effect is studied. By multi-dimensional, multi-scale, and multi-field information fusion, correlation and potential law between fields can be revealed. The unobservable abnormal vibration and noise can be represented by observable DC disturbance and load factor. The multi-parameter correlation method is validated through consistency between simulation and experiments, which provides a foundation for digital twin technology in full lifecycle management.

ACKNOWLEDGEMENT

The authors want to thank the National Key R&D Program of China (2021YFB2400802) for their strong support.

APPENDIX A.

As shown in Fig. A1, the arrangement of magnetic domains is irregular when the magnetic field intensity **H** is 0. However, the ferromagnetic material is magnetized when a magnetic field exists in the external environment. In this case, the internal magnetic domains will move in the same direction so that the length of the ferromagnetic material will increase ΔL. The change in the length of the iron core material is indicated by magnetostrictive coefficient ε.

$$\varepsilon = \frac{\Delta L}{L} \tag{A1}$$

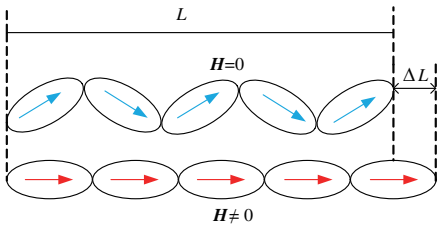

FIGURE A1. Principle of magnetostrictive effect.

Considering the magnetostrictive effect, the relationship among relative permeability, tensile stress, and magnetic flux density are described as follows.

$$\Delta\mu = -\frac{2\varepsilon_m \sigma \mu^2}{\mathbf{B}_m^2} \tag{A2}$$

$$\mathbf{B}_\sigma = (\mu + \Delta\mu)\mathbf{H} + \varepsilon\sigma \tag{A3}$$

where μ is the magnetic permeability. $\Delta\mu$ is the relative permeability. σ is the tensile stress. ε_{m} is the magnetostrictive coefficient in magnetic saturation condition. $\mathbf{B}_{\mathrm{m}}$ is the saturation magnetic flux density. $\mathbf{B}_\sigma$ is the magnetic flux density with tensile stress.

APPENDIX B.

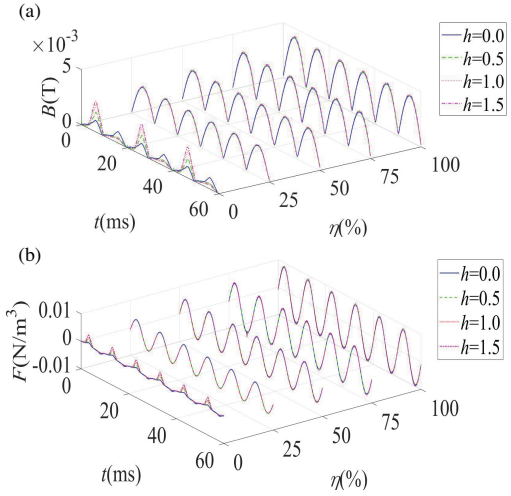

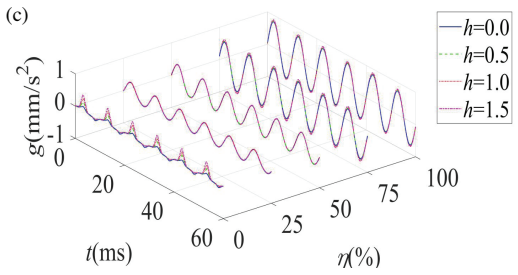

FIGURE B1. Partial simulation results of three-phase group transformer winding. (a) Leakage at measuring point 7. (b) Force at measuring point 8. (c) Acceleration at measuring point 8.

REFERENCES

[1] Zhao, X. J., Z. M. Jin, G. Wang, and F. Xiao, "Analysis of three-phase three-limb transformer under asymmetrical DC bias by using frequency-domain decomposition based on complex exponential," *Proc. CSEE*, Vol. 39, No. 4, 1206–1215, Feb. 2019.

[2] Wang, A., S. Lin, Z. Hu, J. Li, F. Wang, G. Wu, and Z. He, "Evaluation model of DC current distribution in AC power systems caused by stray current of DC metro systems," *IEEE Transactions on Power Delivery*, Vol. 36, No. 1, 114–123, Feb. 2021.

[3] Pan, Z., X. Wang, B. Tan, L. Zhu, Y. Liu, Y. Liu, and X. Wen, "Potential compensation method for restraining the DC bias of transformers during HVDC monopolar operation," *IEEE Transactions on Power Delivery*, Vol. 31, No. 1, 103–111, Feb. 2016.

[4] Canturk, S., M. E. Balci, M. H. Hocaoglu, and A. K. Koseoglu, "Investigation of the effects of DC bias on single-phase shell type transformers using frequency-dependent reluctance-based model," *IEEE Transactions on Magnetics*, Vol. 57, No. 9, 1–9, Sep. 2021.

[5] Chen, Z., H. Li, L. Liu, L. Xiang, and B. Bai, "DC bias treatment of hybrid type transformer based on magnetic flux modulation mechanism," *IEEE Transactions on Magnetics*, Vol. 55, No. 6, 1–4, Jun. 2019.

[6] Xie, Z., X. Lin, Z. Zhang, Z. Li, W. Xiong, H. Hu, M. S. Khalid, and O. S. Adio, "Advanced DC bias suppression strategy based on finite DC blocking devices," *IEEE Transactions on Power Delivery*, Vol. 32, No. 6, 2500–2509, Dec. 2017.

[7] Li, X., X. Wen, P. N. Markham, and Y. Liu, "Analysis of nonlinear characteristics for a three-phase, five-limb transformer under DC bias," *IEEE Transactions on Power Delivery*, Vol. 25, No. 4, 2504–2510, Oct. 2010.

[8] Chen, D., B. Hou, Z. Feng, and B. Bai, "Study of magnetostriction influence of electrical sheet steel under different DC biases," *IEEE Transactions on Magnetics*, Vol. 55, No. 2, 1–5, Feb. 2019.

[9] He, J., Z. Yu, R. Zeng, and B. Zhang, "Vibration and audible noise characteristics of AC transformer caused by HVDC system under monopole operation," *IEEE Transactions on Power Delivery*, Vol. 27, No. 4, 1835–1842, Oct. 2012.

[10] Hu, J., D. Liu, Q. Liao, Y. Yan, and S. Liang, "Analysis of transformer electromagnetic vibration noise based on finite element method," *Transactions of China Electrotechnical Society*, Vol. 31, No. 15, 81–88, Aug. 2016.

[11] Zhu, L., Q. Yang, R. Yan, and X. Zhan, "Research on vibration and noise of power transformer cores including magnetostriction effects," *Transactions of China Electrotechnical Society*, Vol. 28, No. 4, 1–6, Apr. 2013.

[12] Li, B., Z. Z. Wang, X. J. Zhao, H. B. Liu, H. M. Li, and J. B. Liu, "Experimental on vibro-acoustic characteristic of 500 kV three-phase group transformer under DC-bias," *Transactions of China Electrotechnical Society*, Vol. 36, No. 13, 2801–2811, Jul. 2021.

[13] Zhao, X., J. Lu, L. Li, Z. Cheng, and T. Lu, "Analysis of the DC bias phenomenon by the harmonic balance finite-element method," *IEEE Transactions on Power Delivery*, Vol. 26, No. 1, 475–485, Jan. 2011.

[14] Liu, X., J. Wu, H. Lin, A. Jadoon, and J. Wang, "Research on DC bias analysis for transformer based on vibration Hilbert Huang transform and ground-state energy ratio method," *International Journal of Electrical Power & Energy Systems*, Vol. 109, 73–82, Jul. 2019.

[15] Pan, C., C. Wang, Z. Liu, and X. Chen, "Winding vibration analysis of unbalanced transformer based on electromagnetic-mechanical coupling," *International Journal of Electrical Power & Energy Systems*, Vol. 134, Jan. 2022.

[16] Zhang, F., S. Ji, L. Naranpanawe, H. Ma, C. Ekanayake, T. Saha, and L. Zhu, "Investigation of overall and local vibration characteristics of disk-type windings," *IET Generation Transmission & Distribution*, Vol. 14, No. 18, 3685–3691, Sep. 2020.

[17] Chao, P., X. Chen, and G. Cai, "Mode-state characteristics of three-phase unbalanced operation winding vibration of transformer based on electromagnetic mechanical coupling principle," *Proceedings of the CSEE*, Vol. 40, No. 14, 4695–4707, Jul. 2020.

[18] Ben, T., F. Chen, and L. Chen, "An improved magnetostrictive model of non-oriented electrical steel sheet considering force-magnetic coupling effect," *Proceedings of the CSEE*, Vol. 41, 5261–5370, Aug. 2021.

[19] Chen, Z., Q. Zhou, G. Ding, X. Wu, J. Wu, and Y. Zhang, "Influence of magnetic state variation on transformer core vibration characteristics and its measurement," *IEEE Transactions on Instrumentation and Measurement*, Vol. 71, 1–8, 2022.

[20] Tanzer, T., H. Pregartner, M. Riedenbauer, R. Labinsky, M. Witlatschil, A. Muetze, and K. Krischan, "Magnetostriction of electrical steel and its relation to the no-load noise of power transformers," *IEEE Transactions on Industry Applications*, Vol. 54, No. 5, 4306–4314, Sep.-Oct. 2018.

[21] Power transformers-Part 10: Determination of sound levels, International Standard, IEC 60076-10, 2001.